Computational Fluid Dynamics Analysis of the Venturi Dustiness Tester

Prahit Dubey,

Mechanical and Materials Engineering, College of Engineering and Applied Science, University of Cincinnati, Cincinnati, Ohio 45221-0072

Urmila Ghia, and

Mechanical and Materials Engineering, College of Engineering and Applied Science, University of Cincinnati, Cincinnati, Ohio 45221-0072

Leonid A. Turkevich[*]

Chemical Exposure and Monitoring Branch (CEMB), Division of Applied Research and Technology (DART), National Institute for Occupational Safety and Health (NIOSH), Centers for Disease Control and Prevention (CDC), 1090 Tusculum Avenue, Cincinnati, Ohio 45226

Abstract

Dustiness quantifies the propensity of a finely divided solid to be aerosolized by a prescribed mechanical stimulus. Dustiness is relevant wherever powders are mixed, transferred or handled, and is important in the control of hazardous exposures and the prevention of dust explosions and product loss. Limited quantities of active pharmaceutical powders available for testing led to the development (at University of North Carolina) of a Venturi-driven dustiness tester. The powder is turbulently injected at high speed ($Re \sim 2 \times 10^4$) into a glass chamber; the aerosol is then gently sampled ($Re \sim 2 \times 10^3$) through two filters located at the top of the chamber; the dustiness index is the ratio of sampled to injected mass of powder. Injection is activated by suction at an Extraction Port at the top of the chamber; loss of powder during injection compromises the sampled dustiness. The present work analyzes the flow inside the Venturi Dustiness Tester, using an Unsteady Reynolds-Averaged Navier-Stokes formulation with the k-ω Shear Stress Transport turbulence model. The simulation considers single-phase flow, valid for small particles (Stokes number Stk <1). Results show that ~ 24% of fluid-tracers escape the tester before the Sampling Phase begins. Dispersion of the powder during the Injection Phase results in a uniform aerosol inside the tester, even for inhomogeneous injections, satisfying a necessary condition for the accurate evaluation of dustiness. Simulations are also performed under the conditions of reduced Extraction-Port flow; results confirm the importance of high Extraction-Port flow rate (standard operation) for uniform distribution of fluid tracers. Simulations are also performed under the

[*]Corresponding Author: LLT0@cdc.gov, Tel.: 513-841-4518, Fax : 513-841-4545.

conditions of delayed powder injection; results show that a uniform aerosol is still achieved provided 0.5 s elapses between powder injection and sampling.

Search terms

Dustiness of Powders; Dustiness Methods; Venturi Dustiness Tester; Computational Fluid Dynamics

Additional Keywords

Reynolds-Averaged Navier-Stokes Equations; Euler-Lagrange Method; Round Jet Impingement; Aerosol

1. INTRODUCTION

1.1. Dustiness

The measurement of dustiness has received renewed interest in the powder and occupational health communities as a test relevant for the assessment of exposure to particulates. Historically, dustiness tests were intended to simulate typical environmental and occupational settings so that an assessment could be made of exposure and a recommendation could be made as to a level of control [1–5]. Unfortunately, no clear relationship has yet been established linking inhalation exposure to dustiness as determined by any of these historical methods [1–2, 4, 6–11]. This may be due to the gentle nature of the tests employed, as well as to the variability of the external parameters, which influence the test.

Dustiness is relevant wherever powders are mixed, poured [12–13], transferred [14], handled, or conveyed [15] and is important in the control of hazardous exposures. Aerosol resuspension from dusty surfaces [16] is relevant for the prevention of dust explosions [17–19]. Sanding [20], grinding or milling of bulk materials generates and suspends small particles as airborne dusts [5]. Dust is also ubiquitous in mining and agricultural settings [21].

1.1.1. Dustiness Testing—Dustiness quantifies the propensity of a finely divided solid to be aerosolized by a prescribed mechanical stimulus. The aerosolization process overcomes the adhesive binding forces within the powder and thus disperses pre-existing particles from the powder into the air [22–23]. A dustiness test is not intended to comminute the powder and generate new particles. This precludes the use of high shear critical orifices [24] and high impact processes [25] for dustiness determination.

Several attempts have been made at standardization [26–28], but these have not been widely accepted.

1.1.2. Historical dustiness test methods: falling powder and rotating drum— Historically [29–32], dustiness testing has utilized configurations (falling powder, rotating drum) that have imparted fairly gentle mechanical agitation to the powder. While these tests

were devised to simulate various industrial procedures, their gentle agitation may be responsible for difficulties in reproducibility, as external factors must then be stringently controlled. The maximum velocities of the particles achieved are $v \sim 1$ m/s, and the aerodynamics tend to involve large-scale eddies. These techniques typically require the use of relatively large quantities of powder, e.g., $10^2 - 10^3$ grams per test [28].

In the falling powder method, a bolus of particles is released from a height [27]. The particles are aerosolized either by the countercurrents generated during the fall, or by the countercurrents generated by the impact of the bolus at the bottom of the fall [6, 14, 33–41].

In the rotating drum (Heubach) method, a powder is rotated within a drum with internal baffles; again, the particles are aerosolized by the countercurrents generated during the periodic avalanches [42–48].

These methods have been compared using a variety of powders [22, 49–53]. Modeling of the aerosolization and dust generation under these test conditions has also been attempted [54–56]. Dustiness measurement using a gas fluidization technique has also been proposed [57–58].

1.1.3. Venturi Dustiness Tester (VDT)—A qualitatively different method was introduced [59] in order to test pharmaceutical powders. Evans *et al.* [60] used this method to study a wide variety of nanoscale powders. The aim was to utilize small quantities (~ 5 mg) of powder under confined conditions (both for reproducibility and so as to limit exposure of the test operator to potentially toxic material) [61]. Similar measurements have recently been made on pollens and molds [62].

A powder is introduced into a dispersion chamber under energetic turbulent airflow conditions; typical nozzle airflow $v \sim 70$ m/s. Aerosolization presumably occurs via aerodynamic lift and pneumatic drag mechanisms acting on the powder; particulate velocities are one to two orders of magnitude larger than in the gentler falling powder and rotating drum methods. Aerosolization proceeds under turbulent conditions, whereas in the gentle tests, the airflows are larger scale and laminar. The reproducibility [59] of the method has been criticized [63] but has been defended [64]. The method involves more aggressive air flows than those typically encountered in large-scale workplace activities (however, the use of compressed air to clean contaminated worker clothing or work surfaces approximates the aerodynamic conditions of the VDT).

Each of these methods is under consideration [65] as a potential ISO standard test method of dustiness (falling powder and rotating drum [Annex C], and the Venturi method [Annex E]).

1.2. Geometry of the Venturi Dustiness Tester (VDT)

Figure 1 is a schematic of the VDT. It consists of a 5.7 L glass dispersion chamber with a square base and a tapered top. The horizontal end of an inverted tee-shaped injection tube (*d* = 0.44 cm) pierces the midsection of the front wall (Nozzle Inlet); powder is aerosolized within this tee-shaped tube and enters the VDT as an aerosolized jet. The VDT has three outflow ports: an Extraction Port, a Sampler Port (Dust Sampler), and a Cyclone Port

(Respirable Mass Cyclone). During the Injection Phase, air is drawn out of the VDT through the Extraction Port; this is closed during the Sampling Phase. In both the Injection and Sampling Phases, the Dust Sampler collects powder particles of all sizes on its filter cassette, and the Cyclone collects respirable dust (particles less than 4.25 µm in diameter) on its filter.

1.3. Experimental Operation of the VDT

Prior to the start of the experiment, the powder, mass M_t, is loaded in the Inlet Nozzle. Operation of the VDT consists of two phases, Injection and Sampling. During the Injection Phase, at $t = 0$, flow is set up in the Extraction Port, Cyclone, and Sampler, at the rates of $Q_{ep} = 53.8$ L/min, $Q_{cp} = 4.2$ L/min, $Q_{sp} = 2.0$ L/min, respectively. These flow rates are continued until $t = 1.50$ s. The balanced replacement flow enters through the Nozzle at $Q_{in} = 60.0$ L/min, giving rise to an inlet velocity $v = 65.80$ m/s, corresponding to a Reynolds number $Re_d = 19,900$ (based on the hydraulic diameter of the nozzle). During the Sampling Phase ($t > 1.50$ s), the Extraction Port is closed (while the inlet and the Cyclone and Sampler ports remain open), reducing the total replacement flow to $Q_{in} = 6.2$ L/min. This is continued for 240 s, during which the inlet flow rate corresponds to an inlet velocity $v = 6.79$ m/s and $Re_d = 2,050$.

At the end of the experiment, each filter is removed and weighed. The masses of the powder collected on the cyclone filter, M_{dc}, and on the dust sampler, M_{ds}, are used to calculate [59–60] the respirable and total dustiness, respectively, as

$$D_{resp} = \frac{Q_{in}}{Q_{cp}} * \frac{M_{dc}}{M_t} \quad (1)$$

$$D_{tot} = \frac{Q_{in}}{Q_{sp}} * \frac{M_{ds}}{M_t} \quad (2)$$

1.4. Need for Computational Fluid Dynamics (CFD) Analysis of the VDT

Absent a modeling analysis, the VDT remains somewhat of a 'black box'. A CFD analysis will elucidate the aerodynamics of the VDT so as to better understand the robustness of the instrument and its operating protocol. We are particularly interested in understanding whether the instrument is effective in uniformly dispersing powders (Injection Phase), whether the sampling is statistically sound or subject to biases, and whether the dustiness estimates (1) and (2) are accurate.

We first study the aerodynamics of the standard operation of the instrument (Injection and Sampling Phases). We next examine the effects of reduced injection flows, and of inhomogeneous and delayed powder injections. In these studies, we assume that the Venturi and aerodynamic drag mechanisms are effective in aerosolizing the powder (which occurs in the Nozzle prior to entering the VDT); we confine ourselves to the fate of that aerosol once it has entered the VDT.

2. CFD ANALYSIS OF THE VENTURI DUSTINESS TESTER

2.1. Mathematical Formulation

For the flow entering the VDT, $Re_d \approx 19{,}900$, during the Injection Phase, and $Re_d \approx 2050$, during the Sampling Phase, both in the turbulent regime [66]. Therefore, the CFD simulations have been conducted as Unsteady-Reynolds-Averaged Navier-Stokes (URANS), using a Shear-Stress k-ω turbulence model [67–69]. The equations were solved numerically using a finite-volume pressure-based solver (Fluent 14.5), using SIMPLE (semi-implicit method for pressure-linked equations) [70] as the pressure–velocity coupling method, with the default values for the relaxation parameters (0.3 for continuity and 0.7 for momentum). Convective and diffusion terms are integrated in space using a second-order upwinding scheme, and a second-order accurate central-differenced scheme, respectively. Temporal discretization was performed using a second-order accurate implicit scheme. Trapezoidal numerical integration is employed to calculate the fluid-tracer trajectories.

The continuity and momentum (Reynolds-averaged Navier-Stokes) equations are given by:

$$\frac{\partial (u_j)}{\partial x_i} = 0 \quad (3)$$

$$\frac{\partial (\rho u_i)}{\partial t} + \frac{\partial (\rho u_i u_j)}{\partial x_j} = -\frac{\partial p}{\partial x_i} + \frac{\partial}{\partial x_j} \left\{ \mu \left(\frac{\partial u_i}{\partial x_j} + \frac{\partial u_j}{\partial x_i} - \frac{2}{3} \delta_{ij} \frac{\partial u_1}{\partial x_1} \right) \right\} + \frac{\partial}{\partial x_j} \left(-\rho \overline{u_i' u_j'} \right) \quad (4)$$

where $-\rho \overline{u_i' u_j'}$ represent Reynolds stresses, and unprimed, u_i, and primed, u_i', denote, respectively, averaged and fluctuating velocities (summation convention over repeated indices).

Within the Boussinesq approximation, the Reynolds stresses are given by the mean velocity gradients:

$$-\rho \overline{u_i' u_j'} = \mu_t \left(\frac{\partial u_i}{\partial x_j} + \frac{\partial u_j}{\partial x_i} \right) - \frac{2}{3} \left(\rho k + \mu_t \frac{\partial u_k}{\partial x_k} \right) \delta_{ij}. \quad (5)$$

Here k and μ_t are, respectively, the turbulent kinetic energy and turbulent viscosity, with appropriate transport equations [67–69]; ρ is the fluid density, and δ_{ij} is the Kronecker delta.

2.1.1. Convergence criteria—The solution of the equations was considered to be converged when the scaled residuals for the continuity, momentum, turbulent kinetic energy, and specific dissipation-rate equations decreased to 10^{-5} for each time step ($t_{injection} = 10^{-4}$ s, $t_{sampling} = 10^{-3}$ s) during the simulation.

2.1.2. Fluid-tracer Tracking—The aerosol is modeled by massless fluid-tracers, which follow the local fluid flow (Lagrangian framework); the tracer velocity, v_t, is same as the velocity of the fluid, v_f. Fluid-tracer trajectories are calculated by integrating

$$\frac{dx_t^k}{dt} = v_t^k \quad (6)$$

Fluid streamlines never intersect the walls, so additional wall boundary conditions are not needed for the particles (fluid-tracers); thus, there are no wall losses.

2.1.3. Statistics of Fluid-tracer Concentration—To assess the homogeneity of the aerosol, the VDT chamber volume is divided into 90 regions ('boxes') of roughly equal volume (the box map is detailed in Supplemental Material Fig. S2), and the fluid-tracer population in each box is monitored; from this population map, a concentration histogram is constructed. A spatially uniform concentration corresponds to a narrow concentration distribution, with a sharply transitioning cumulant; a broad distribution, with a gently transitioning cumulant, indicates concentration inhomogeneities.

2.2. Mesh Generation

Mesh generation plays a significant role in numerical convergence and solution accuracy. For the VDT, a sufficiently dense mesh is required to resolve the shear layer region of the inlet nozzle jet. In addition, there should be enough cells in the jet impingement region. Sufficient mesh resolution of the boundary layers on the walls and high gradient regions near the outlet ports is also necessary.

2.2.1. Refinement near walls—In order to resolve the turbulent boundary layer, and successfully implement near-wall turbulence modeling, the mesh must be refined [71] near the walls (Enhanced Wall Treatment). Near the walls, the mesh cell size is determined [72] using $y^+ \sim 1$, where

$$y^+ = \frac{yu^*}{v}, \text{and where } u^* = \sqrt{\frac{\tau_w}{\rho}} \quad (7)$$

Structured prism-cell layers are used on the walls. For $y^+ = 1$, the cell size is 0.1 mm. This transitions to the bulk domain (filled with tetrahedral elements) over eight structured prism layers, with a geometric progression of 1.1.

2.2.2. Refinement around aerosol jet—A coarse mesh cannot resolve the gradient of the velocity (and other turbulent flow properties) around the jet. An iso-geometric mesh is used inside and around the jet shear layer (Fig. 2). The jet width, *b*, is expected [66, 73–74] to increase linearly with axial distance, *x*, as *b = 0.11 * x*. Inside this conical refinement region, tetrahedral elements of size 0.4 mm (front half of the jet) and 0.8 mm (back half of the jet), connected linearly over 4 layers, are used. The conical refinement region again transitions to the bulk domain with tetrahedral elements increasing in size with a geometric progression 1.05. The enhanced flow near the Extraction Port is treated with a similar mesh refinement.

The total number of mesh points is $\sim 3 \times 10^6$.

Grid independence of the simulation results is addressed in the Supplemental Material.

2.3. Conditions for Applicability of Simulations

2.3.1. Condition for particles to follow streamlines—A particle (massless fluid tracer in these simulations) will follow the local streamline if [75] the corresponding Stokes number, $Stk < 1$. For a particle of diameter, d_p, and density, ρ_p, moving in a fluid of viscosity, μ_f, the Stokes number, $Stk \sim \rho_p \, d_p^2 \, v/18 \, \mu_f \, D$, where D is a characteristic length [75–76]. Near the nozzle, $v \sim 65.76$ m/s, $D \sim 2$ mm; for $d_p \sim 1$ μm, with $\rho_p \sim 2.5$ g/cm^3 (typical of inorganic solids), $Stk \sim 0.3$. The Stokes number needs to be modified in turbulent flow [75, 77–78].

2.3.2. Condition for Incompressibility—The maximum velocity $v = 65.76$ m/s occurs at the Nozzle during injection. This corresponds to a Mach number $Ma = v/c_{sound} \sim 0.19$ (where $c_{sound} = 340$ m/s is the speed of sound in air). It is thus appropriate to treat the flow in the VDT as incompressible [76].

2.3.3. Condition for Dilute Aerosol—For a powder (density $\rho_p \sim 2.5$ g/cm^3) with spherical particles of diameter $d_p \sim 1$ μm, if all 5 mg is aerosolized in the tube ($D = 2$ mm, $L = 2$ cm), the volume fraction occupied by the powder is $\phi_{tube} \sim 10^{-1}$, so the average distance between particles is $n^{-1/3} \sim 2$ μm, which is comparable to the particle size. Thus, within the Nozzle, the aerosol is definitely not dilute. Within the cone of the jet, $\phi_{cone} \sim 1.5 \times 10^{-3}$, so the distance between particles is $n^{-1/3} \sim 10$ μm. Once the aerosol is homogeneously dispersed within the VDT, the volume fraction occupied is $\phi_{box} \sim 3 \times 10^{-7}$, so the distance between particles is $n^{-1/3} \sim 120$ μm, which is quite dilute. Thus, aside from inside the Nozzle, the aerosol is dilute throughout the Injection Phase.

2.3.4. Condition for Neglecting Gravitational Settling—Comparing the gravitational settling velocity, v_{grav}, to a typical velocity, v, in the flow, $v_{grav}/v \sim Stk \, L/v^2$. Within the Sampling Phase, $v_{inlet} \sim 7$ m/s, $Stk \sim 0.03$, $L \sim 17$ cm, whence $v_{grav}/v \sim 10^{-3}$, and gravitational settling may be neglected. During the Injection Phase, typical velocities are higher, so, again, gravitational settling may be neglected.

3. RESULTS AND DISCUSSION

This section presents the results of the numerical simulations. Flow visualization, using fluid-tracers, enables an understanding of the aerosol dynamics during the Injection Phase, and evaluation of the spatial distribution of the aerosol at end of Injection Phase, the depletion of the aerosol during the Sampling Phase, and the spatial distribution of the aerosol at the end of the Sampling Phase. To quantify the fluid-tracer distribution, the VDT is divided into 90 small volume boxes (Fig. S2), and fluid-tracer number concentration is determined as a function of time in each of these boxes; aerosol inhomogeneity is quantified by the spatial statistics of the concentration. Fluid-tracers are followed from the Injection Nozzle to either collection (on the Sampler or the Cyclone) or exit (through the Extraction Port); this permits an estimate of fluid-tracer loss during the Injection Phase.

3.1. Flow Analysis of Standard VDT Operation

3.1.1. Injection Phase—The flow rates used in this simulation correspond to the standard operation of the VDT. Motivated by the experimental visualization [60] of powder injection into the VDT, fluid-tracers are continuously released during the first sixth of the Injection Phase ($0 < t < 0.24$ s). Throughout the Injection Phase (1.50 s), all three exit ports (Extraction, Cyclone, Sampler) remain open; the flow is balanced by the total inlet flow through the Injection Nozzle, $Q_{in} = 60$ L/min ($Re_d = 19{,}900$).

Figures 3a, b show the flow evolution inside the VDT during the Injection Phase, which is remarkably similar to the experimental visualization of aerosol injection (Figure 2 of [60]).

Figure 3a details the aerosol flow during the first quarter of the Injection Phase; the aerosol jet is directed towards the back wall of the VDT; the edges of the jet roll back due to opposing viscous forces [79]. The jet impinges on the back wall at $t \sim 0.01$ s, and starts to spread radially on the wall; this is recognized as normal impingement of a circular jet on a plane surface [74, 80–81]. The interaction of the jet with the wall results in the formation of ring-shaped wall eddies ($t = 0.03$ s), which are associated [79] with enhancement of local momentum transfer. These eddies roll up and progress radially ($t = 0.06$ s) until they reach the bottom and top edges of the VDT. Experimentally, powder from the nozzle only impacts the back wall at t ~ 0.20 s (Fig. 2f of [60]); the ring-shaped eddy is evident at t ~ 0.33 s (Fig. 2i of [60]).

Asymmetry between top and bottom (due to the protruding Samplers) results in the formation of two slightly different flow patterns in the VDT. Near the bottom edge of the VDT, the interaction of the ring-shaped wall eddies with the bottom wall results in the formation of larger vortices. Flow around the left and right edges starts to move backwards, resulting in aerosol circulation from the back half to the front half of the VDT ($t = 0.12$ s. 0.18 s. 0.24 s). At $t = 0.30$ s, aerosol at the bottom half of the VDT is entrained by the jet, thus completing one circulation. This circulation is primarily responsible for mixing and the eventual uniform aerosol distribution within the VDT.

A slightly different flow pattern develops in the top half of the VDT due to the presence of the Cyclone, Sampler, and Extraction Ports. Aerosol first reaches the Extraction Port at $t = 0.12$ s. Remaining aerosol starts to move backwards along the top and sidewalls. The two sampling devices (Cyclone and Dust Sampler) obstruct this backward motion, thus forcing the aerosol to move through the region between the Cyclone and the Sampler, and close to the sidewalls. In particular, the obstruction posed by the Cyclone results in a higher concentration of aerosol in the region behind the Cyclone. At $t = 0.36$ s, flow in the top half of the VDT is entrained by the incoming jet, thus completing one circulation.

Experimentally, the ring-shaped wall-eddies do not seem to persist for as long as the simulation indicates; e.g. there is no evidence of any remnant large-scale recirculation at t ~ 0.77 s (Fig. 2j of [60]).

Figure 3b shows the flow evolution in the VDT during the final three quarters of the Injection Phase. At $t = 0.42$ s, a higher concentration of aerosol is still observed in the

regions around the Cyclone and the Sampler. At subsequent times (t = 0.48 s, 0.54 s, 0.60 s, 0.75 s), incoming fluid from the nozzle continues to stir the aerosol through large-scale structures, thus enhancing aerosol mixing. In the final third of the Injection Phase (t > 1.05 s), the aerosol is uniformly distributed throughout the VDT. Experimentally, the aerosol appears uniform by t ~ 1.50 s (Fig. 2k of [60]).

That the CFD simulation captures the essential features of the experimental VDT powder dispersion is evident if the two processes are compared cinematographically. This may be achieved by viewing the videos in the Appendix.

This uniform aerosol distribution (constant box population—Fig. S3) is confirmed by the sharpness of the cumulant in the fluid-tracer concentration distribution (Fig. 4). The distribution has been normalized to the global density; the distribution at the end of Injection is strongly peaked at the global uniform density; the coefficient of variation $\sigma/\mu = 0.12$ (where μ and σ are, respectively, the mean and the standard deviation of the fluid-tracer distribution).

At the end of the Injection Phase, 23.80% of the injected aerosol has escaped through the Extraction Port (similarly, 0.97% and 0.50% of the aerosol particles have been collected on the Cyclone and Sampler, respectively). Thus, equations (1) and (2) underestimate the true dustiness, as they normalize to the total loaded mass, instead of to the mass available for sampling; thus, the normalizing mass should be replaced by 0.762 M_{td} (the mass which has not escaped through the Extraction Port). Both Respirable and Total Dustiness expressions (1) and (2) should be augmented by the same multiplicative factor 1.312. As this correction factor will undoubtedly engender confusion, it is recommended that experimental work continue to report 'raw' dustiness values, given by equations (1) and (2), but then acknowledge that these must be corrected with the multiplicative factor 1.312 to yield 'injection loss corrected' dustiness values.

Only 2% of the mass collected on each of the Cyclone (0.97/49.10 = 0.02) and the Sampler (0.50/23.49 = 0.02) is deposited during the Injection Phase. Thus, the sampled mass is dominated by the collection during the Sampling Phase and is not biased by any anomalous collection during the Injection Phase.

3.1.2. Sampling Phase—During the Sampling Phase, the Extraction Port is closed while the air is removed through the Cyclone and Sampler Ports. This reduces the total inlet flow rate of air to Q_T = 6.2 L/min (v_{inlet} = 6.79 m/s, Re_d = 2,050). During the Sampling Phase (240 s), material is collected on the Sampler and the Cyclone. For this simulation, the initial condition is the final flow condition and fluid-tracer distribution obtained at the end of the Injection Phase. Figures 5a and 5b show the decay of aerosol concentration in the VDT and the accumulation of aerosol passing through Sampler and Cyclone, respectively. Initially (t < 80 s), the aerosol concentration decays exponentially

$$\frac{N^*(t)}{N_i^*} = e^{-\frac{t}{\tau}}, \quad (8)$$

consistent with replacement of uniform aerosol by clean air under well-mixed conditions, where $\tau = V/Q_T = 55.16$ s (V is the chamber volume). This compares favorably with the experimental time constant of $\tau = 55.6$ s [60]; in particular, compare the CFD time dependence (Figure 5a) with the experimental time dependence (Figure 3 of [60]). For $t > 80$ s, the spatial distribution of the aerosol inside the VDT is no longer uniform (appearance of dead zones); this leads to a slight retention of aerosol within the VDT above what would be expected from simple dilution: at $t = 240$ s, 3.66% of the aerosol remains in the VDT, compared with 0.96% expected from well-mixed dilution.

At the end of the Sampling Phase, the CFD simulation predicts that 49.10% of the aerosol particles are collected on the Cyclone and 23.49% on the Sampler; 3.66% of the aerosol particles thus remain un-sampled in the VDT. The cumulant of the distribution of fluid-tracer concentration at the end of the Sampling Phase is also shown in Fig. 4. At the end of the Sampling Phase, only a few fluid tracers remain in the VDT. However, the aerosol concentration is not uniform; most regions are devoid of aerosol (low concentration), with a few dead zones (high concentration); the cumulant is thus centered below the global density and exhibits a long tailing at the higher concentrations, reflecting these dead zones. Inspection of the box populations (Supplemental Material Fig. S4) identifies the dead zones as the regions close to the corners or edges.

3.2. Reduction of Extraction-Port Flow Rate

During the standard operation, the Extraction Port draws fluid out at 53.8 L/min, which corresponds to an Extraction-Port Reynolds number $Re_{ep} = 12,200$. As discussed above, 23.8% of the fluid-tracers leave the VDT prior to Sampling. A reduced Extraction-Port flow would reduce this premature loss. However, a reduced Extraction-Port flow might compromise the efficient mixing that results in the uniform distribution of fluid-tracers at the end of Injection. In order to investigate these effects, additional simulations were performed with reduced Extraction-Port flow rates (0.5 Q_{ep}, 0.2 Q_{ep}, 0.1 Q_{ep}).

Operating at reduced Extraction-Port flow rate, $Q_{ep}/2$ ($v_{ep} \sim 33.10$ m/s, $Re_{ep} \sim 6,110$, $v_{inlet} \sim 36.28$ m/s, and $Re_d \sim 10,900$) results in less aerosol (~14.76%) leaving the VDT prior to Sampling. However, the spatial distribution of the aerosol at the end of Injection evinces (Figs. 6 and S5) inhomogeneity (coefficient of variation, $\sigma/\mu = 0.19$).

A further reduction in the Extraction-Port flow rate, $Q_{ep}/10$ ($v_{ep} \sim 2.79$ m/s, $Re_{ep} \sim 1,220$, $v_{inlet} \sim 12.7$ m/s, and $Re_d \sim 3820$), results in still less aerosol (~ 1.20%) escaping the VDT prior to Sampling. However, the spatial distribution of the aerosol at the end of Injection (Figs. 6 and S6) is markedly non-uniform (coefficient of variation, $\sigma/\mu = 0.6$).

Thus, a smaller Extraction-Port flow, Q_{ep}, reduces the loss of aerosol through the Extraction Port during the Injection Phase, but the gentler injection fails to distribute the aerosol uniformly throughout the VDT. A non-uniform distribution of powder will compromise the collection of powders by the Sampler and the Cyclone. Dustiness, as measured in the VDT, presupposes a uniform, well-mixed aerosol during the Sampling Phase. This result cautions against reduction in Q_{ep} below the standard operating conditions.

3.3. Effect of Inhomogeneous Injection

The above study of reduced injection identifies the importance of a uniform aerosol for sampling. In addition to limits on the extraction flow, Q_{ep}, it is also useful to examine how robust the VDT design is to inhomogeneous introduction of powder into the chamber.

In order to understand the effectiveness of this device in producing a spatially uniform aerosol at the end of the Injection Phase, additional cases were run with different fluid-tracer release patterns, but still under the usual injection flow rates As in the standard operation, fluid-tracers are released in the first sixth of Injection ($0 < t < 0.24$ s). Fluid-tracers are released from the left half of the injection nozzle, from the right half of the injection nozzle, from the top half of the injection nozzle, from the bottom half of the injection nozzle, and from a ring bordering the nozzle tube wall. Figure 7 shows the cumulant of the tracer density distribution at the end of the Injection Phase for these various injection scenarios. The detailed flow evolution for these inhomogeneous injections is available in the Supplementary Material.

Again, under the standard operating conditions, at the end of the Injection Phase, aerosol is uniformly distributed throughout the VDT. Thus, inhomogeneous powder injection does not adversely compromise the subsequent sampling; hence, the dustiness measurement is robust against inhomogeneous injection.

3.4. Effect of Delayed Injection

A somewhat different result is obtained if the powder is injected into the VDT after a delay. Additional simulations were performed injecting powder in the intervals 0.6 – 0.9 s, 0.9 – 1.2 s, and 1.2 – 1.5 s. Figure 8 shows the cumulant of the tracer density distribution at the end of the Injection Phase for these various delayed injection scenarios. So long as powder injection occurs in the first two-thirds of the Injection Phase ($t < 1.0$ s), sufficient time elapses before the end of the Injection Phase so that mixing yields a homogeneous tracer distribution prior to the start of Sampling. This lead-time (0.5 s) is comparable to the recirculation time (0.36 s) seen in the flow visualization (Fig. 3a).

3.5. Transition from Injection to Sampling Phases

In order to ascertain how quickly the VDT transitions from the turbulent flow pattern, characteristic of the Injection Phase, to the gentler recirculating flow pattern, characteristic of the Sampling Phase, the mid-plane vorticity (vertical and horizontal), ω, was monitored. This is described in the Supplemental Material (Section S6). Rigorous left-right symmetry and approximate top-bottom symmetry in the circulation (integrated vorticity) is observed. The reduction in total flow, $Q_{sampl} = Q_{inj}/9.68$, is reflected in a corresponding reduction in mid-plane vorticity, ω (240 s) $\sim \omega$ (1.5 s)/9.5. In the simulation, the Extraction-Port flow is turned off abruptly; the vorticity decreases instantaneously, but overshoots and then relaxes to the asymptotic value, with a time constant $\tau = 0.22$ s (bottom and top) and $\tau = 0.26$ s (right and left). This relaxation time is comparable to the circulation time, 0.36 s, observed in the flow visualization of the Injection Phase.

4. CONCLUSIONS

Computational fluid dynamics (CFD) is used to model the aerodynamics of the Venturi Dustiness Tester (VDT). Under the standard operating conditions, 24% of the aerosol is lost during the Injection Phase, which warrants an overall normalization correction to the determination of Respirable and Total Dustiness. The flow visualization confirms the homogenization of the dust in the VDT prior to sampling. During sampling, the dust concentration remains well mixed for most of the dilution, although CFD identified dead zones, where dust accumulates at the end of the Sampling Phase. 98% of the material collected on the Total and Respirable Dust Samplers derives from the Sampling Phase (i.e., only 2% of the material is collected on these filters during the Injection Phase).

CFD was also used to test the robustness of the design and operation with inhomogeneous and delayed injections. Turbulent aerosol injection is shown to be an efficient mechanism for producing a uniform aerosol within the VDT at the end of the Injection Phase. Under the standard operating conditions, the VDT adequately mixes the dust of an inhomogeneous injection. Similarly, delayed injection (up to 0.5 s prior to sampling) of the powder is accommodated by the aggressive mixing in the VDT. However, the instrument is sensitive to reduction in the Extraction-Port flow rate (and, hence, the dispersion flow), as this leads to inadequate homogenization of the aerosol prior to sampling.

Supplementary Material

Refer to Web version on PubMed Central for supplementary material.

Acknowledgments

References

1. Heitbrink WA, Todd WF, Fischbach TJ. Correlation of tests for material dustiness with worker exposure from the bagging of powders. Appl Ind Hyg. 1989; 4:12–16.

2. Heitbrink WA, Todd WF, Cooper TC, O'Brien DM. The application of dustiness tests to the prediction of worker dust exposure. Am Ind Hyg Assoc J. 1990; 51:217–223. [PubMed: 2327332]

3. Mark, D. The use of reliable measurements of dustiness of chemicals in selecting the most appropriate dust control technology. 6th Int. Sci. Conf. Int. Occup. Hyg. Assoc; North West Province, South Africa. 19–23 September 2005; 2005. paper S2–S3

4. Brouwer DH, Links IH, De Vreede SA, Christopher Y. Size selective dustiness and exposure; simulated workplace comparisons. Ann Occup Hyg. 2006; 50:445–452. [PubMed: 16524926]

5. Pensis I, Mareels J, Dahmann D, Mark D. Comparative evaluation of the dustiness of industrial minerals according to European standard EN 15051 (2006). Ann Occup Hyg. 2010; 54:204–216. [PubMed: 19955327]

6. Cowherd C Jr, Grelinger MA, Wong KF. Dust inhalation exposures from the handling of small volumes of powders. Am Ind Hyg Assoc J. 1989; 50:131–138. [PubMed: 2718905]

7. Hofschreuder P, Vrins ELM. Nuisance from coarse dust. J Aerosol Sci. 1992; 23(Suppl 1):S691–S694.

8. Class P, Deghilage P, Brown RC. Dustiness of different high-temperature insulation wools and refractory ceramic fibres. Ann Occup Hyg. 2001; 45:381–384. [PubMed: 11418088]

9. Breum NO, Schneider T, Joergensen O, Rasmussen TV, Eriksen SS. Cellulosic building insulation versus mineral wool, fiberglass or perlite: installer's exposure by inhalation of fibers, dust, endotoxin and fire-retardant additives. Ann Occup Hyg. 2003; 47:653–669. [PubMed: 14602673]

10. Petavratzi E, Kingman SW, Lowndes IS. Assessment of the dustiness and dust liberation mechanisms of limestone quarry operations. Chem Eng Processing. 2006; 46:1412–1423.

11. Tsai C-J, Huang C-Y, Chen SC, Ho C-E, Huang C-H, Chen C-W, Chang C-P, Tsai S-J, Ellenbecker MJ. Exposure assessment of nano-sized and respirable particles at different workplaces. J Nanopart Res. 2011; 13:4161–4172.

12. Sutter SL, Johnston JW, Mishima J. Investigation of accident-generated aerosols: releases from free fall spills. Am Ind Hyg Assoc J. 1982; 43:540–543.

13. Vrins E, Hofschreuder P, Oeseburg F. A field study on the dust emission by coal dumping from a conveyor. J Aerosol Sci. 1988; 19:1385–1387.

14. Heitbrink WA, Baron PA, Willeke K. An investigation of dust generation by free falling powders. Am Ind Hyg Assoc J. 1992; 53:617–624. [PubMed: 1456205]

15. Cheng L. Formation of airborne-respirable dust at belt conveyor transfer points. Am Ind Hyg Assoc J. 1973; 34:540–546. [PubMed: 4770676]

16. Maedler L, Koch W. Particle resuspension from surfaces by impacting objects. J Aerosol Sci. 1997; 28:S85–S86.

17. Cashdollar KL. Overview of dust explosibility characteristics. J Loss Prev Process Ind. 2000; 13:183–199.

18. Turkevich LA, Dastidar AG, Hachmeister Z, Lim M. Potential explosion hazard of carbonaceous nanoparticles—explosion parameters of selected materials. J Haz Mater. 2015; 295:97–103.

19. Turkevich LA, Fernback J, Dastidar AG, Osterberg P. Potential explosion hazard of carbonaceous nanoparticles—screening of allotropes. Combustion and Flame. 2016; 167:218–227. [PubMed: 27468178]

20. Thorpe A, Brown RC. Factors influencing the production of dust during the sanding of wood. J Aerosol Sci. 1992; 23(Suppl 1):S237–S240.

21. Wypych P, Mar L. Investigations into the dustiness of bulk materials. Australian Bulk Handling Review. 2013; 18:64–67.

22. Plinke MA, Maus R, Leith D. Experimental examination of factors that affect dust generation by using Heubach and MRI testers. Am Ind Hyg Assoc J. 1992; 53:325–330. [PubMed: 1609743]

23. Liden G. Dustiness testing of materials handled at workplaces. Ann Occup Hyg. 2006; 50:437–439. [PubMed: 16849593]

24. Ding Y, Riediker M. A system to assess the stability of airborne nanoparticle agglomerates under aerodynamic shear. J Aerosol Sci. 2015; 88:98–108.

25. Froeschke S, Kohler S, Weber AP, Kasper C. Impact fragmentation of nanoparticle agglomerates. J Aerosol Sci. 2003; 34:275–287.

26. ASTM. American Society for Testing and Materials. 1980. Test method for index of dustiness of coal and coke. ASTM. D547–71withdrawn 1986

27. DIN. Deutsches Institut fuer Normung EV (German National Standard). Berlin, Germany: Beauth Verlag; 1999. Determination of a parameter for the dust formation of pigments and extenders—Part 2: Drop Method. DIN 55992-2.

28. CEN. EN 15051 Workplace atmospheres: measurement of the dustiness of bulk materials; requirements and test methods. Brussels, Belgium: European Committee for Standardization; 2006.

29. BOHS. British Occupational Society Technology Committee Working Group on Dustiness Estimation. Dustiness estimation methods for dry materials. In: Hammond, CM.Heriot, NR.Higman, RW.Spivey, AM.Vincent, JH., Wells, AB., editors. Technical Guide No. 4. Science Reviews Ltd; 1985.

30. Hamelmann F, Schmidt E. Methods of estimating the dustiness of industrial powders a review. KONA. 2003; 21:7–18.

31. Hamelmann F, Schmidt E. Methods for characterizing the dustiness estimation of powders. Chem Eng Technol. 2004; 27:844–847.

32. Hamelmann F, Schmidt E. Methods for dustiness estimation of industrial powders. China Particulology. 2005; 3:90–93.

33. Andreasen AHM, Hoffman-Bang H, Rasmussen NH. On the ability of materials to be dusty. Kolloid-Zeitschrift. 1939; 86:70–77.

34. Hammond CM. Dust control concepts in chemical handling and weighing. Ann Occup Hyg. 1980; 23:95–109. [PubMed: 7377672]

35. Lundgren DA. A measurement technique to quantitate fugitive dust emissions from handling granular products. J Aerosol Sci. 1986; 17:632–634.

36. Lundgren DA, Rangaraj CN. A method for the estimation of fugitive dust emission potentials. Powder Technology. 1986; 47:61–69.

37. BOHS. Progress in dustiness estimation. Ann Occup Hyg. 1988; 32:535–544.

38. Plinke MA, Leith D, Holstein DB, Boundy MG. Experimental examination of factors that affect dust generation. Am Ind Hyg Assoc J. 1991; 52:521–528. [PubMed: 1781432]

39. Cawley B, Leith D. Bench-top apparatus to examine factors that affect dust generation. Appl Occup Environ Hyg. 1983; 8:624–631.

40. Plinke MAE, Leith D, Boundy MG, Loeffler F. Dust generation from handling powders in industry. Am Ind Hyg Assoc J. 1995; 56:251–257.

41. Wells AB, Alexander DJ. A method for estimating the dust yield of powders. Powder Technology. 1978; 19:271–277.

42. Chung KY, Burdett GJ. Dustiness testing and moving towards a biologically relevant dustiness index. Ann Occup Hyg. 1994; 38:945–949. [PubMed: 7825934]

43. Hjemsted K, Schneider T. Time dependent dust release during dustiness testing. J Aerosol Sci. 1993; 24(Suppl 1):S251–S252.

44. Hjemsted K, Schneider T. Dustiness from powder materials. J Aerosol Sci. 1996; 27:S485–S486.

45. Hjemsted K, Schneider T. Documentation of a dustiness drum test. Ann Occup Hyg. 1996; 40:627–643.

46. Breum NO, Nielsen BH, Nielsen EM, Midtgaard U, Poulsen OM. Dustiness of compostable waste: a methodological approach to quantify the potential of waste to generate airborne micro-organisms and endotoxin. Waste Manag Res. 1997; 15:169–187.

47. Breum NO. The rotating drum tester; variability in dustiness relation to sample mass, testing time, and surface adhesion. Ann Occup Hyg. 1999; 43:557–566.

48. DIN. Deutsches Institut fuer Normung EV (German National Standard). Berlin, Germany: Beauth Verlag; 2006. Determination of a parameter for the dust formation of pigments and extenders—Part 1: Rotation Method. DIN 55992-1.

49. Heitbrink WA. Factors affecting the Heubach and MRI dustiness tests. Am Ind Hyg Assoc J. 1990; 51:210–216. [PubMed: 2327331]

50. Carlson KH, Herman DR, Markey TF, Wolff RK, Dorato MA. A comparison of two dustiness evaluation methods. Am Ind Hyg Assoc J. 1992; 53:448–454.

51. Bach S, Schmidt E. Determining the dustiness of powders—a comparison of three measuring devices. Ann Occup Hyg. 2008; 52:717–725. [PubMed: 18927102]

52. Schneider T, Jensen KA. Combined single-drop and rotating drum dustiness test of fine to nanosize powders using a small drum. Ann Occup Hyg. 2008; 52:23–34. [PubMed: 18056087]

53. Jensen KA, Koponen IK, Clausen PA, Schneider T. Dustiness behaviour of loose and compacted bentonite and organoclay powders. What is the difference in exposure risk? J Nanopart Res. 2009; 11:133–146.

54. Plinke MAE, Leith D, Goodman RG, Loeffler F. Particle separation mechanisms in flow of granular material. Particulate Sci Technol. 1994; 12:71–87.

55. Plinke MAE, Leith D, Loeffler F. Cohesion in granular materials. Bulk Solids Handling. 1994; 14:101–106.

56. Lanning JS, Boundy MG, Leith D. Validating a model for the prediction of dust generation. Particulate Sci Technol. 1995; 13:105–116.

57. Sethi SA, Schneider T. A gas fluidization dustiness tester. J Aerosol Sci. 1996; 27(Suppl 1):S305–S306.

58. Sethi SA. Generation of small particles by gas fluidization. J Aerosol Sci. 1997; 28(Suppl 1):S539–S540.

59. Boundy M, Leith D, Polton T. Method to evaluate dustiness of pharmaceutical powders. Ann Occup Hyg. 2006; 50:453–458. [PubMed: 16484334]

60. Evans DE, Turkevich LA, Roettgers CT, Deye GJ, Baron PA. Dustiness of fine and nanoscale powders. Ann Occup Hyg. 2013; 57:261–277. [PubMed: 23065675]

61. Heron RJL, Pickering FC. Health effects of exposure to active pharmaceutical ingredients. Occup Med. 2003; 53:357–362.

62. Turkevich LA, Ashley E, Matin N, Fernback J. Dustiness of pollens and molds. unpublished.

63. Bach S, Eickmann U, Schmidt E. Comparison of established systems for measuring the dustiness of powders with the UNC dustiness tester developed especially for pharmaceutical substances. Ann Occup Hyg. 2013; 57:1078–1086. [PubMed: 23749502]

64. Evans DE, Turkevich LA, Roettgers CT, Deye GJ. Comment on 'Comparison of dustiness methods'. Ann Occup Hyg. 2014; 58:524–528. [PubMed: 24477891]

65. ISO. ISO TC 229 working draft (ISO TC 229/SC N--ISO/PDTS 12025). 2012. Nanomaterials—Quantification of nano-object release from powders by generation of aerosols.

66. Bejan, A. Convection Heat Transfer. 3. Hoboken, NJ: John Wiley and Sons, Inc; 2004.

67. Menter FR. Two-equation eddy-viscosity turbulence models for engineering applications. AIAA Journal. 1994; 32:1598–1605.

68. Menter FR. Review of the shear-stress transport turbulence model--experience from an industrial perspective. Int J Comp Fluid Dynamics. 2009; 23:305–316.

69. Wilcox, DC. Turbulence Modeling for CFD. 3. La Canada, CA: DCW Industries, Inc; 2006.

70. Patankar, SV. Numerical Heat Transfer and Fluid Flow. Washington, DC: Hemisphere Publishing Corp., McGraw-Hill; 1980.

71. Salim, SM., Cheah, SC. Wall y^+ strategy for dealing with wall-bounded turbulent flows. In: Ao, SI.Castillo, O.Douglas, C.Feng, DD., Lee, JA., editors. Proceedings of the International MultiConference of Engineers and Computer Scientists. Vol. 2. Vol. 2175. 2009. p. 2165-2170.Lecture Notes in Engineering and Computer Science

72. Fox, RW., Pritchard, PJ., McDonald, AT. Introduction to Fluid Mechanics. 7. Hoboken, NJ: John Wiley & Sons, Inc; 2009.

73. Lee, JHW., Chu, V. Turbulent Jets and Plumes: A Lagrangian Approach. Norwell, MA: Kluwer Academic Publishers; 2003.

74. Belataos S, Rajaratnam N. Impinging circular turbulent jets. J Hydraulics Div. 1974; 100:1313–1328.

75. Hinds, WC. Aerosol Technology: Properties, Behavior, and Measurement of Airborne Particles. 2. New York: John Wiley and Sons Inc., New York; 1999. section 5.3

76. Baron, PA., Willeke, K. Gas and Particle Motion. In: Baron, PA., Willeke, K., editors. Aerosol Measurement: Principles, Techniques, and Applications. 2. Vol. chapter 4. New York: Wiley-Interscience; 2001. p. 61-82.

77. Hagiwara, Y. Local Stokes number for particles in turbulent flow. 7th Int. Conf. Multiphase Flow. ICMF 2010; Tampa, FL. 30 May–4 June 2010; 2010.

78. Mercer, TT. Aerosol Technology in Hazard Evaluation. New York: Academic Press; 1973.

79. Popiel CO, Trass O. Visualization of a free and impinging round jet. Exp Thermal Fluid Sci. 1991; 4:253–264.

80. Bradshaw, P., Love, EM. The Normal Impingement of a Circular Air jet on a Flat Surface. Aero Research Council; England: 1959. R and M no. 3205

81. Fitzgerald JA, Garimella SV. A study of the flow field of a confined and submerged impinging jet. Int J Heat Mass Transfer. 1997; 41:1025–1034.

APPENDIX—POWDER DISPERSION VIDEOS

Courtesy of D.E.Evans, G.J. Deye, P.A. Baron (deceased)

This appendix contains two videos, which amplify the discussion of Section 3.1.1. The first video illustrates the experimental dispersal of TiO2 powder in the Venturi Dustiness Tester.
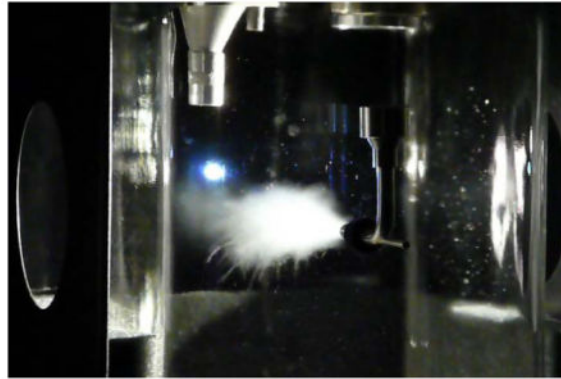
Still images from this video were reported in [60]. The second video 'animates' the CFD simulation of powder dispersion in the injection phase, under standard operating conditions of the instrument (Figure 3).
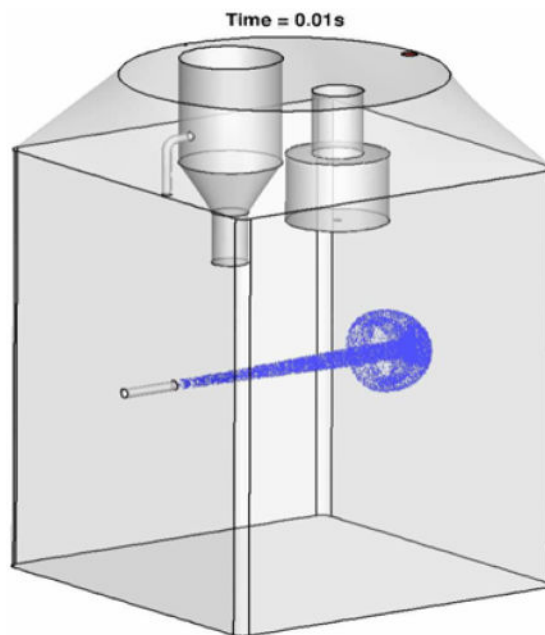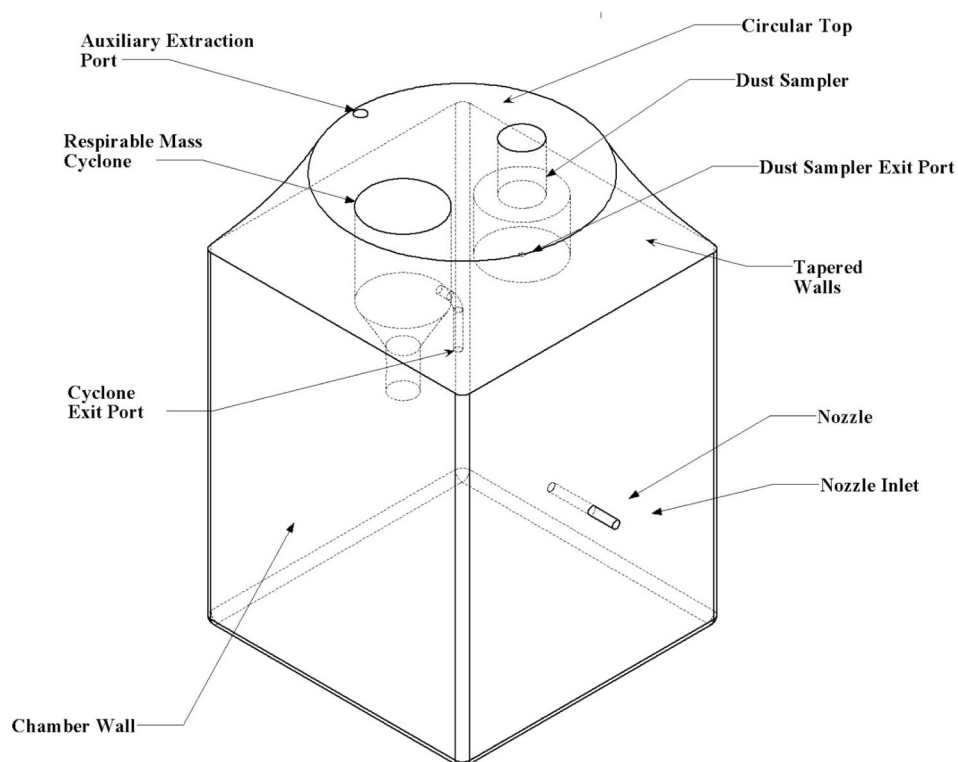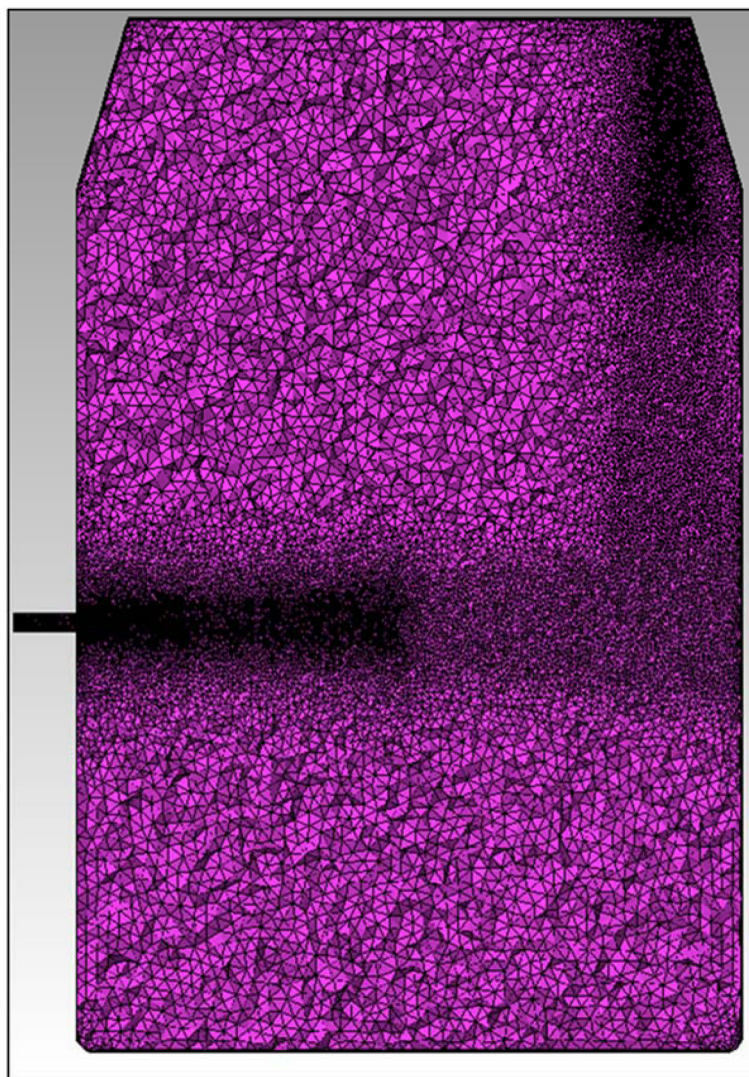
FIGURE 1.
Schematic of the Venturi Dustiness Tester

FIGURE 2.
Generated mesh at axial plane, showing refinement around aerosol jet and Extraction Port

Figure 3a
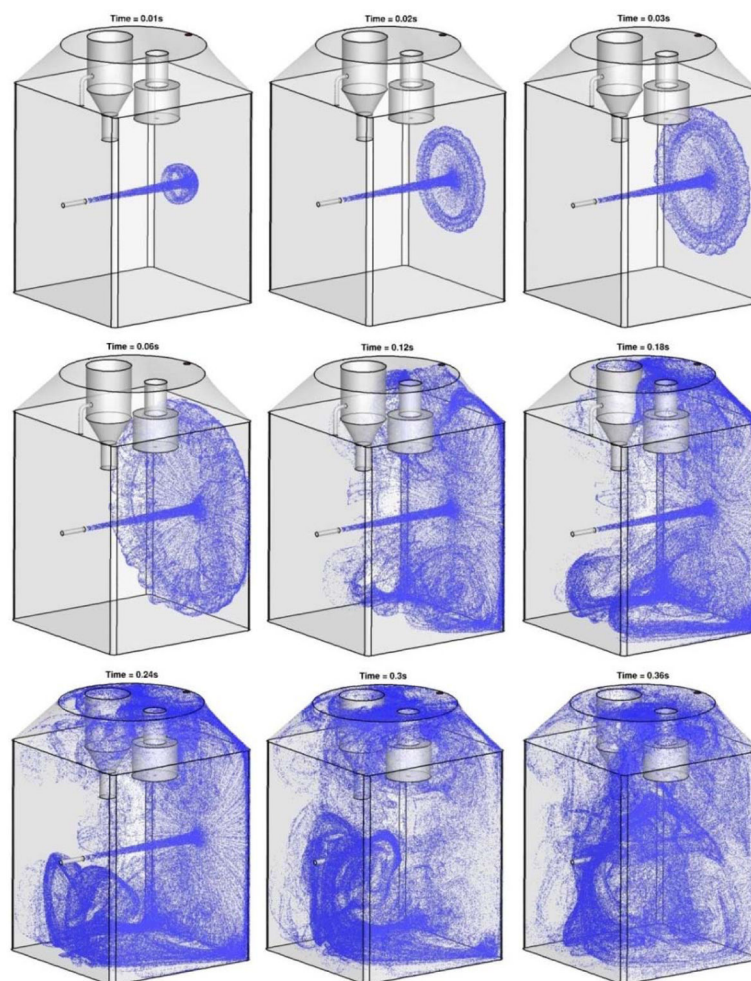
Figure 3b
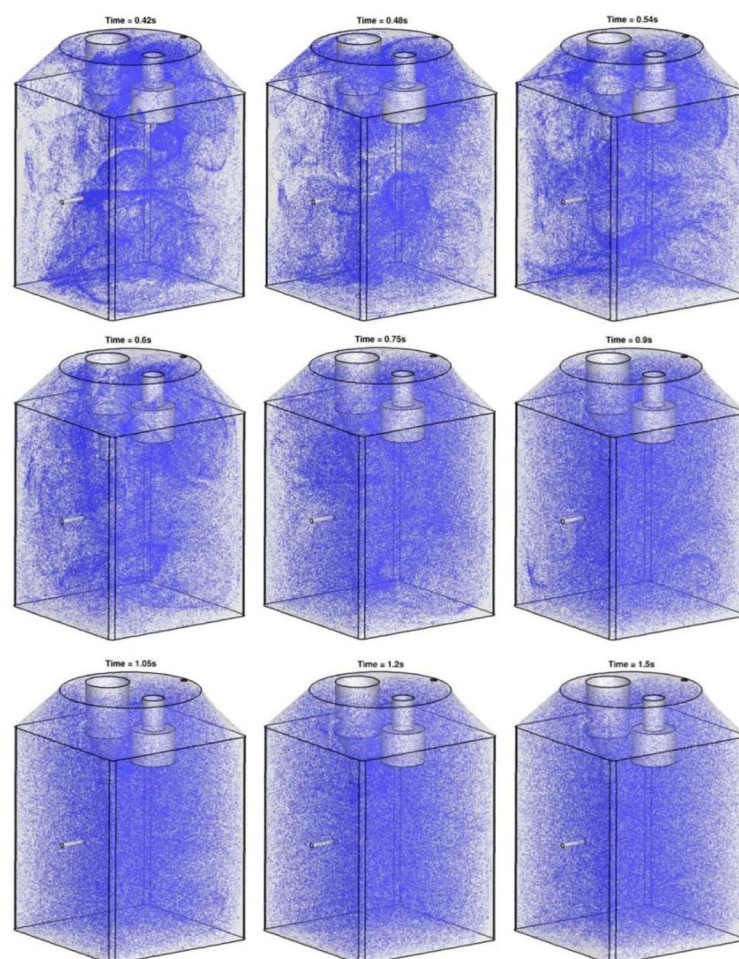
FIGURE 3.
FIGURE 3a. Time Evolution of Fluid-Tracers during Injection Phase (t = 0.01s, 0.02s, 0.03s, 0.06s, 0.12s, 0.18s, 0.24s, 0.30s, 0.36s)
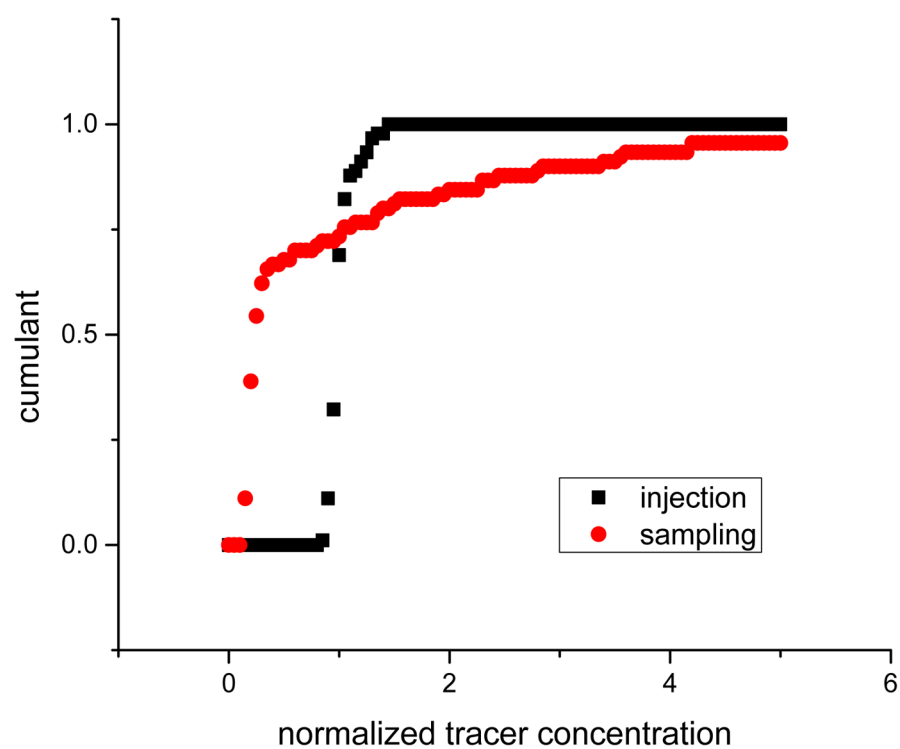FIGURE 3b. Time Evolution of Fluid-Tracers during Injection Phase (t = 0.42s, 0.48s, 0.54s, 0.60s, 0.75s, 0.90s, 1.05s, 1.20s, 1.50s)

FIGURE 4.
Cumulant of tracer concentration distribution at the end of Injection (black) and Sampling (red) Phases. The particle density has been normalized to the global mean density.
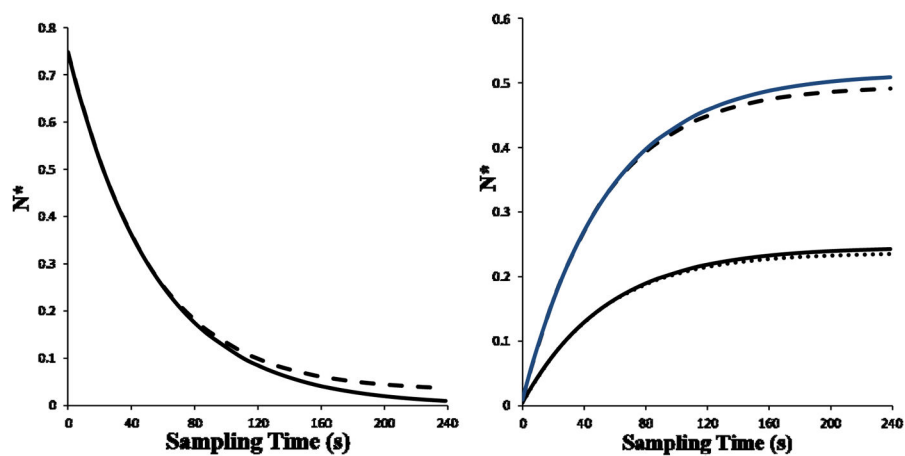
FIGURE 5.
a) Decay of Fluid-Tracer Number in VDT during Sampling Phase;
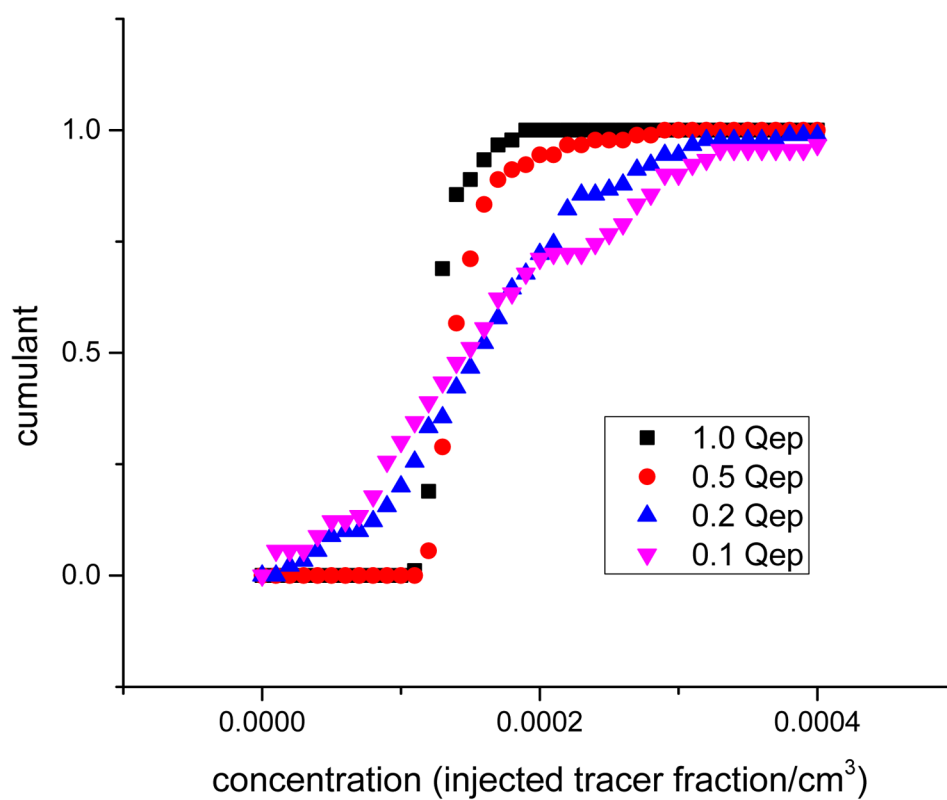b) Cumulative Number of Fluid-Tracers passing through Cyclone and Sampler during Sampling Phase

FIGURE 6.
Cumulant of tracer density distribution at the end of Injection (1.5 s) for different injection rates
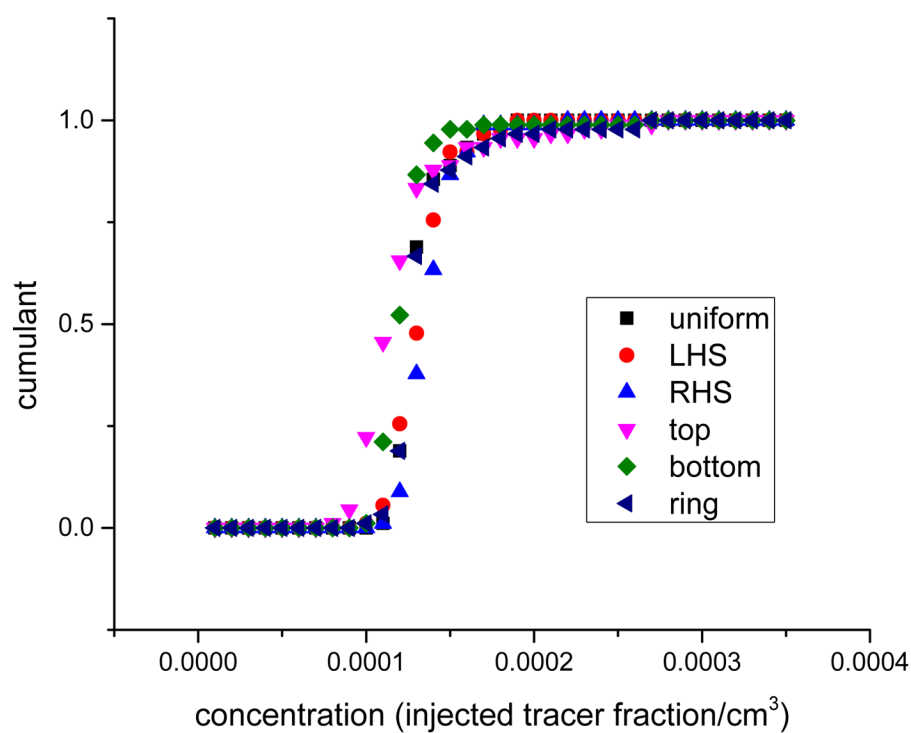
FIGURE 7.
Cumulant of tracer density distribution at the end of Injection (1.5 s) for various injection scenarios
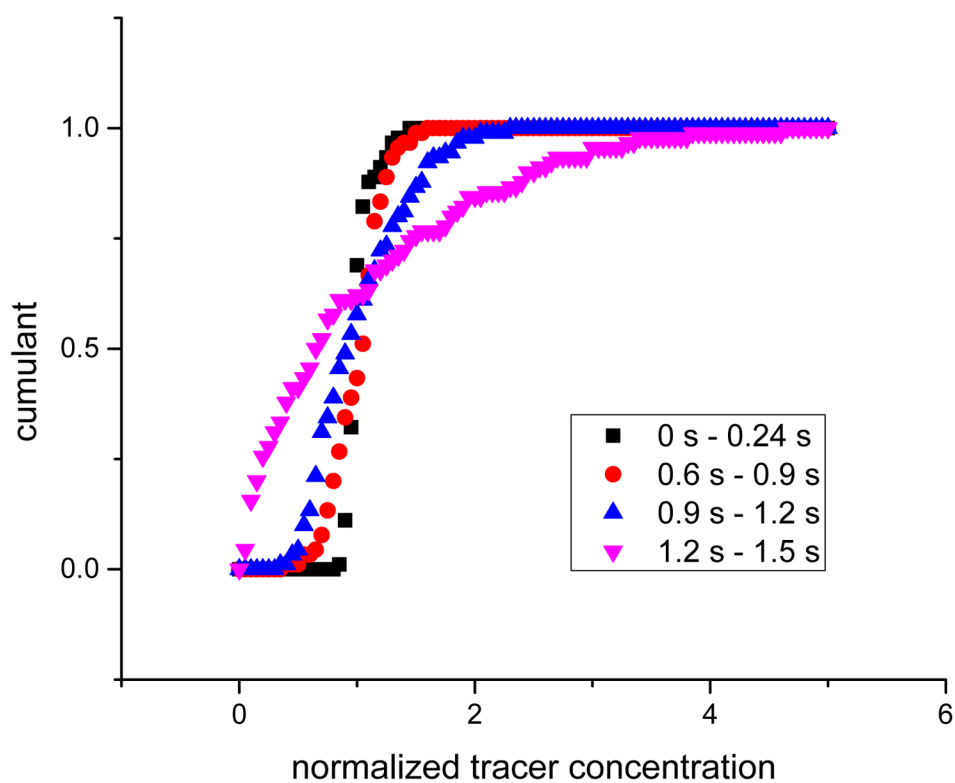
FIGURE 8.
Cumulant of tracer density distribution at the end of Injection (1.5 s) for various delayed injection scenarios